Characterization of a microwave-excited atmospheric-pressure argon plasma jet using two-parallel-wires transmission line resonator

J. Choi, I. S. Eom, S. J. Kim, Y. W. Kwon, H. M. Joh, B. S. Jeong, and T. H. Chung

Citation: Physics of Plasmas **24**, 093516 (2017); doi: 10.1063/1.4989728
View online: http://dx.doi.org/10.1063/1.4989728
View Table of Contents: http://aip.scitation.org/toc/php/24/9
Published by the American Institute of Physics

Characterization of a microwave-excited atmospheric-pressure argon plasma jet using two-parallel-wires transmission line resonator

J. Choi,[1] I. S. Eom,[2] S. J. Kim,[2] Y. W. Kwon,[2] H. M. Joh,[2] B. S. Jeong,[3] and T. H. Chung[2,a)]
[1]*Advanced Manufacturing Process R&D Group, Korea Institute of Industrial Technology, Ulsan 44413, Korea*
[2]*Department of Physics, Dong-A University, Busan 49315, Korea*
[3]*Department of Electronic Engineering, Dong-A University, Busan 49315, Korea*

(Received 11 June 2017; accepted 25 August 2017; published online 11 September 2017)

This paper presents a method to produce a microwave-excited atmospheric-pressure plasma jet (ME-APPJ) with argon. The plasma was generated by a microwave-driven micro-plasma source that uses a two-parallel-wire transmission line resonator (TPWR) operating at around 900 MHz. The TPWR has a simple structure and is easier to fabricate than coaxial transmission line resonator (CTLR) devices. In particular, the TPWR can sustain more stable ME-APPJ than the CTLR can because the gap between the electrodes is narrower than that in the CTLR. In experiments performed with an Ar flow rate from 0.5 to 8.0 L·min^{-1} and an input power from 1 to 6 W, the rotational temperature was determined by comparing the measured and simulated spectra of rotational lines of the OH band and the electron excitation temperature determined by the Boltzmann plot method. The rotational temperature obtained from OH(A-X) spectra was 700 K to 800 K, whereas the apparent gas temperature of the plasma jet remains lower than ~325 K, which is compatible with biomedical applications. The electron number density was determined using the method based on the Stark broadening of the hydrogen H_β line, and the measured electron density ranged from 6.5×10^{14} to 7.6×10^{14} cm^{-3}. TPWR ME-APPJ can be operated at low flows of the working gas and at low power and is very stable and effective for interactions of the plasma with cells. *Published by AIP Publishing.* [http://dx.doi.org/10.1063/1.4989728]

I. INTRODUCTION

Non-thermal atmospheric-pressure plasmas (APPs) have diverse industrial and biomedical applications[1,2] such as sterilization,[3] cancer treatment,[4] and fuel reforming.[5] Microwave-excited APP sources have unique features and potential.[6] Microwave-excited plasmas have several advantages over low-frequency plasmas: high density of electrons and reactive species, low breakdown powers, low heavy-particle temperatures, and lower discharge voltages.[7–9] Furthermore, the mean energy of the ion flux which reaches the electrode decreases as the driving frequency increases.[10] APP devices that work with microwave power generally have low sheath voltage, low power dissipation, and long operational lifetime.[11] In particular, the microwave-excited resonator that uses transmission lines (TLs) can operate with high power efficiency.[7,12]

A variety of APP sources with TL resonators use a coaxial transmission line,[7,12] a micro-strip line,[13] or a parallel plate transmission line.[14] Because the APPs or microwave-excited atmospheric-pressure plasma jets (ME-APPJs) that use TL resonators have different characteristics in size, shape, and plasma physics, the TL resonators can be designed and customized according to the purpose of use. Microwave-driven TL resonators can be made palm-sized due to the high frequency operation. Furthermore, a simplified microwave model of the plasma impedance can be easily drawn and analyzed to verify that the power efficiency of the TL resonator increases in the presence of ME-APPJ.[7,11,12] As a result, an optimized microwave power module for ME-APPJ can be manufactured, even in integrated circuits or on a single chip, so ME-APPJ can be operated using batteries. However, the TL resonators are difficult to fabricate and must be tuned after assembly. Thus, for effective and stable generation of the ME-APPJ, the structure of APP devices that use TL resonators must be simplified.

This paper reports a microwave-excited plasma generator at atmospheric pressure based on a two-parallel-wire transmission line resonator (TPWR). The TPWR is designed and fabricated in a manner similar to a previous report.[12] To ensure that the device operates at resonance, its length is a quarter-wavelength at the operational frequency of ~1 GHz. Due to the simple configuration, the TPWR is easier to fabricate and adjust than the coaxial transmission line resonator (CTLR). Moreover, the TPWR sustains stable ME-APPJ because the gap between the electrodes can be designed to be $<500\ \mu$m while maintaining the 50-Ω characteristic impedance Z_0 of a two-parallel-wire transmission line. The TPWR for ME-APPJ was manufactured as follows: First, an analytic solution based on the microwave theory was obtained to determine the appropriate location of power feeds to dispense with the need for extra matching circuits. Second, a numerical analysis with COMSOL Multiphysics was performed to confirm the calculation and to design the TPWR. The electric field intensity generated by the TPWR was estimated by simulation. Finally, the actual device was fabricated and characterized.

For characterization, the gas temperature was measured using a fiber optic temperature sensor, and the optical

a)Author to whom correspondence should be addressed: thchung@dau.ac.kr

characteristics of the ME-APPJ with the TPWR were investigated. The electron excitation temperature was estimated by using the Boltzmann plot, and the rotational temperature was determined by comparing the measured and simulated spectra of rotational lines of the OH band. The electron density was obtained based on Stark broadening of the H_β spectral line profile of the measured emission spectra. Then, a chemical probe method was used to measure the reactive species generated in the ME-APPJ treated liquids. The TPWR ME-APPJ was applied to plasma treatment on cells *in-vitro* to assess its applicability in biomedicine.

II. DESIGN OF THE TPWR

TPWR is composed of a two-parallel-wire transmission line that uses air as a dielectric and a connector. The TPWR is short-circuited at one end and electrically open at the other end, where l_1 is the distance from the short port of the TPWR to the feeding point and l_2 is the distance from the feeding point to the open port of the TPWR [Fig. 1(a)]. To operate at resonance, the lengths of the two wires are one-quarter the wavelength of the operation frequency of ~900 MHz. The electric field intensity is the highest at the open port of the resonator, where the plasma is generated. The Z_0 value of the two-parallel-wire transmission line is determined by the characteristic impedance η_0 of free space, the dielectric constant ε_r of air, the diameter d of the wires, and the distance D between their centers [Fig. 1(b)]:

$$Z_0 = \frac{\eta_0}{\pi\sqrt{\varepsilon_r}} \cosh^{-1}\left(\frac{D}{d}\right). \quad (1)$$

In this work, $Z_0 = 50\ \Omega$, so $d = 6.5$ mm and $D = 7$ mm.[15] Consequently, the gap s, where the plasma is ignited, is 0.5 mm. The microwave power is coupled into the device via a subminiature type A (SMA) connector [Fig. 1(a)].

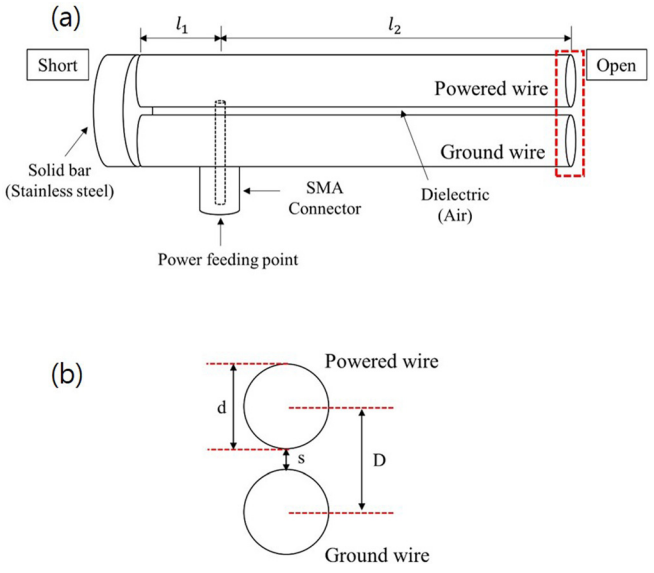

FIG. 1. Schematic of the TPWR: (a) configuration of the TPWR and (b) cross-section of two-parallel wires and design parameters of the transmission line. $d = 6.5$ mm and $D = 7$ mm, gap s where the plasma is ignited is 0.5 mm, l_1 is the distance from the short port of the TPWR to the feeding point, and l_2 is the distance from the feeding point to the open port of the TPWR.

After the analytic solution was found using the equation of input impedance for a quarter-wavelength resonator,[16] numerical analysis was performed with the commercial software to confirm the calculation. The simulation domain and electric field estimation of the TPWR (Fig. 2) consider two parallel wires and the SMA connector to investigate microwave propagation and reflection coefficient S_{11} at resonant frequency f_0 of the TPWR with COMSOL Multiphysics based on the finite element method [Fig. 2(a)].[17] The feeding point to transfer maximum power was tuned by changing the location of the SMA connector in the simulation. The electric field at the open port of the TPWR with an input power of $P_{IN} = 0.01$ W was estimated to be 1.14×10^4 V·m^{-1} [Fig. 2(b)]. P_{IN} is defined as the net microwave power, i.e., the difference between incident power to the TPWR and reflected power from the TPWR. Considering the simulation result of the electric field, the TPWR can generate the APP with increasing P_{IN} up to a few watts by using either an additional metal tip or an extra ignitor.[16] The extra ignitor does not significantly affect the matching condition of the TPWR until the APP has been ignited at the open end of the device.

III. FABRICATION AND EXPERIMENTAL SETUP

A. Fabrication of the TPWR

The TPWR was designed and manufactured to operate at 1 GHz (Fig. 3). For the given frequency, the quarter-wavelength $\lambda/4 = L = l_1 + l_2 = 75$ mm, which is the same as the length of the two-parallel-wire transmission line of the resonator. Both electrodes of the TPWR are made of stainless steel 304. A solid bar of stainless steel 304 (ST1 Co.) was used for the short-circuit at the end of the TPWR. The bar was welded to be tight to the wires. A hole was drilled through the solid bar to enable the working gas flow into the

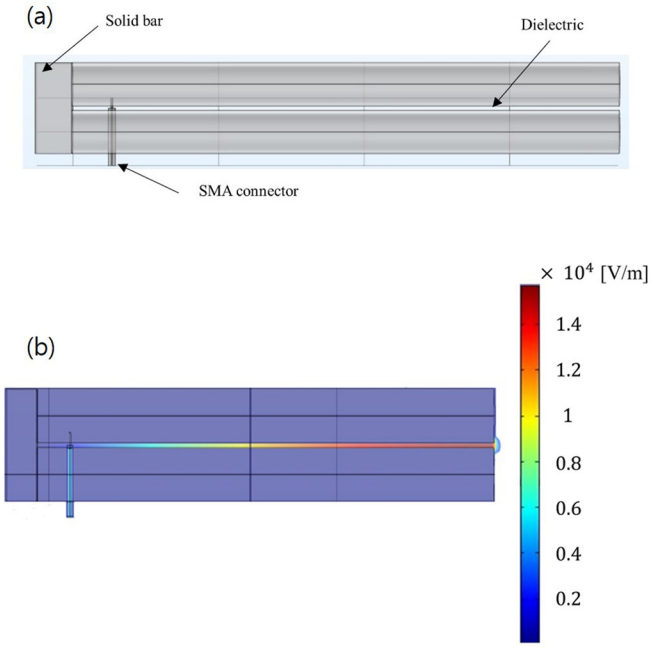

FIG. 2. Electric field analysis of the TPWR: (a) simulation domain of the TPWR with COMSOL and (b) result of electric field distribution with an input power of 0.01 W.

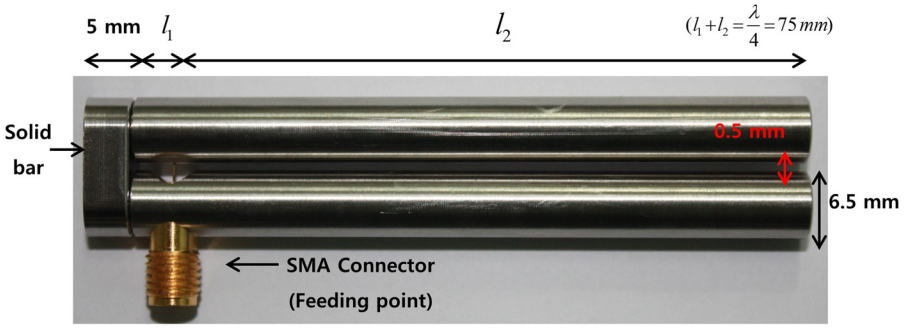

FIG. 3. Configuration of TPWR for operation at 1 GHz.

gap between two parallel wires. An SMA connector (PSF-S03-000-1cc, Gigalane Co.) that uses Teflon as a dielectric was installed to couple the microwave power. The inner and outer conductors of the SMA connector were made of beryllium copper and stainless steel, respectively. The ground wire of the TPWR was machined to join the SMA connector. Then, the microwave power was applied by connecting the center pin of the SMA connector to the powered wire. It was manufactured to minimize the disturbance caused by the SMA connector. The same material properties were considered in simulations.

Specific parameters (Table I) of the TPWR were summarized at each stage (e.g., finding an analytic solution of the power feeding location, conducting the simulation, and fabricating the device). For all processes, the length of the resonator was 75 mm, air ($\varepsilon_r \approx 1.0$) is applied to the two-parallel-wires transmission line as a dielectric, and Z_0 was designed to be 50 Ω. Theoretically, the power-feeding point to the TPWR, where no matching circuit is necessary, was found to be $l_1 = 3.0$ mm. Computations demonstrated that the optimal location of the feeding point is $l_1 = 5.4$ mm. Based on the simulation result, the actual device was manufactured and tuned to find the optimal feeding point. However, the device is likely to be modified from the initial design. For the best power efficiency of the fabricated resonator, the optimal condition where the value of S_{11} is minimum should be found. Hence, the location of the feeding point was determined by moving the position along the TL, as a matter of convenience, while fixing the length of the resonator. For instance, as l_1 was changed to 4, 5.6, and 9.3 mm, S_{11} and the resonant frequencies differed significantly [Fig. 4(a)]. Eventually, the feeding point of the device manufactured was determined to be 5.6 mm (Fig. 3). Furthermore, the reflection coefficients by the simulation with COMSOL and the measurement using a network analyzer were compared [Fig. 4(b)]. The f_0 values for the analytic solution, simulation, and fabrication were 1 GHz, 960 MHz, and 920 MHz, respectively (Table I). Because precise implementation of the device according to the theoretical calculation and the design parameter is difficult, f_0 is likely to vary slightly.

TABLE I. Specific parameters of the TPWR for analytic solution, simulation, and fabrication.

	Analytic solution	Simulation	Fabrication
Length of device ($l_1 + l_2$)	75 mm	75 mm	75 mm
Dielectric material	Air	Air	Air
Characteristic impedance Z_0	50 Ω	50 Ω	50 Ω
l_1	3.0 mm	5.4 mm	5.6 mm
l_2	72 mm	69.6 mm	69.4 mm
Resonant frequency f_0	1 GHz	960 MHz	920 MHz

B. Experimental setup

The experimental setup is similar to a previous report.[13] A signal generator (Agilent E8251A) and a linear power RF amplifier (OPHIR RF 5016A) were used to supply power to the TPWR. The incident and reflected powers were monitored using two directional couplers (CK-68N), power sensors (E9300A), and power meters (E4416A). The resonant frequency and reflection coefficient of the device were

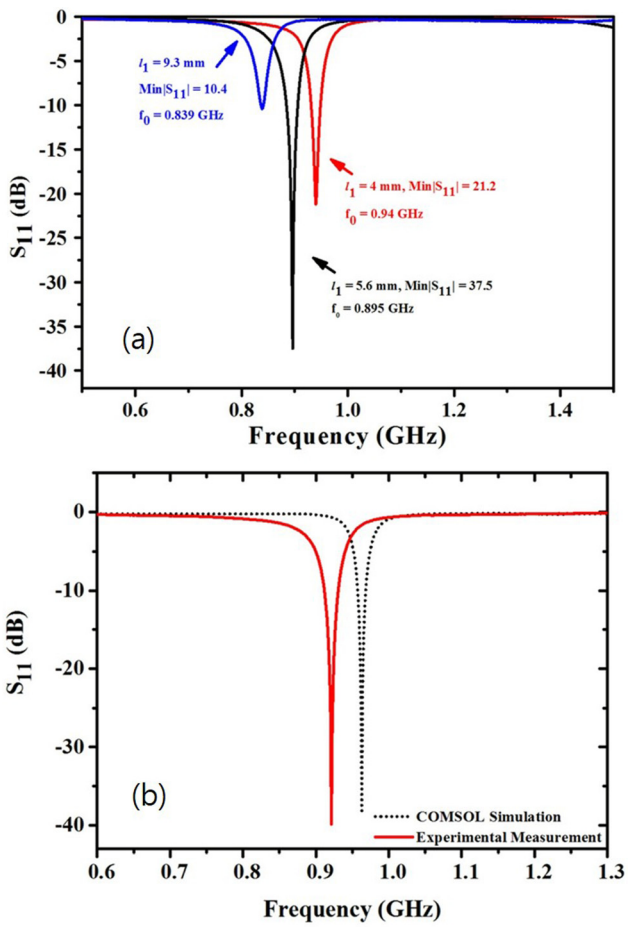

FIG. 4. Measurement of reflection coefficients (S_{11}): (a) change in the S_{11} and resonant frequencies (f_0) at different locations of the feeding point and (b) comparison between simulation and experiment of S_{11}.

measured using a network analyzer (HEWLETT PACKARD 8753D), and the optical emission spectrum of the APP was measured using two kinds of spectrometers: a photodiode-array spectrometer (Ocean Optics USB2000+XR1-ES) and monochromator (SPEX 1702) with a photomultiplier tube (PMT) (Hamamatsu R928). A microwave power of up to 10 W was supplied directly to the TPWR from the signal generator and power amplifier. As shown in Fig. 5, the TPWR was covered by the acrylic case for gas feeding. The operating gas (Ar) flows into the acrylic case which envelops the TPWR to concentrate the Ar gas at the open end of the resonator. The plasma jet was used to treat the liquid samples or cancer cells in Petri dishes. The gas temperature T_G was measured using a fiber-optic temperature sensor (Luxtron M601-DM&STF).

To identify excited species in the plasma jet, optical emission spectra were obtained using a simple photodiode-array spectrometer. To obtain fine structured rotational bands of OH and to measure Stark broadening, a higher resolution spectrometer is used. The light emitted by the plasma was focused with a lens (focal length, 30 mm; diameter, 12 mm) onto an optical fiber into an entrance slit of a 0.75 m monochromator, equipped with a grating of 1200 grooves per millimeter and a slit width of 80 μm. The light was collimated at the exit slit where a photomultiplier tube converted photons into an electric signal. As shown in Fig. 5, an optical fiber is directed perpendicular to the open end of the electrodes and the distance to the plasma is about 50 mm (plasma – focusing lens – optical fiber end). The detection system was calibrated in intensity using a quartz halogen lamp with a known spectral radiance.

OH· is one of the most active species generated in moist gas mixtures. Knowing the production mechanisms and measuring the absolute density of OH species will help guide adjustment of treatment doses and allow for the optimization of the plasma process for specific applications.[18] OH radicals detected in the plasma-treated liquid originate mainly in the gas phase although some OH generation is possible at the liquid interface by photo-dissociation of water molecules by UV emitted by the plasma jet. The electron-impact reactions including those by plasma-activated neutral species contribute strongly to the generation of OH species in the gas phase. The OH in the gas phase spreads into the liquid phase and reacts with water to produce various biologically active reactive species. The presence of H_2O_2 accelerates the decomposition of ozone and increases the concentration of OH radicals in water.[19]

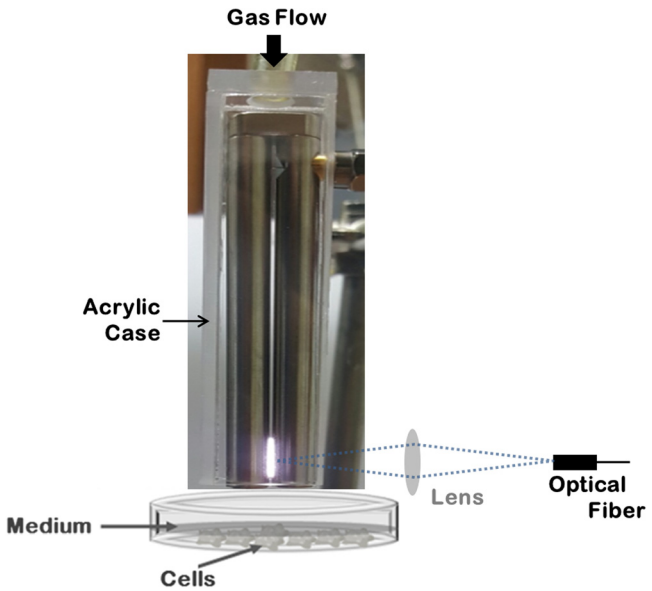

FIG. 5. Photograph of the Ar TPWR ME-APPJ covered by the acrylic case for gas feeding.

As a method to detect OH radicals, we used the hydroxylation of terephthalic acid (TA) because this process is a typical photocatalytic reaction that specifically oxidizes TA. The OH radical reacts with TA to form hydroxyterephthalic acid (HTA), which fluoresces. When the solution containing TA and HTA molecules is irradiated by UV, the HTA molecules emit light at $\lambda = 425$ nm, whereas TA molecules do not.[20] An LED light source (Ocean Optics, $\lambda = 310$ nm and FWHM, 10 nm) was used to excite hydroxyterephthalic acid (HTA) in a cuvette, and the spectrum near $\lambda = 425$ nm was recorded through an optical fiber by using a spectrometer. An aqueous solution of TA was prepared by dissolving TA (Sigma) in distilled water containing NaOH (Wako). The initial concentrations of TA and NaOH were 3 mM and 10 mM, and the initial pH was 8. The dish plate (diameter, 20 mm) including liquids was irradiated with the plasma (for 5 min), and samples of the liquids from dish after plasma treatment were taken using a cuvette to observe the fluorescence after exciting by the light source. The fluorescent signals were converted into concentrations using an authentic 2HTA external standard. A series of 2HTA dilutions in NaOH solution was made to generate a calibration curve over the range of 0.5–100 μM.[20]

To investigate the *in-vitro* cellular effect induced by plasma treatment, we treated melanoma (Hs 895.T) cells using a microwave jet plasma. The cells were maintained in Dulbecco's Modification of Eagle's Medium (DMEM) and supplemented with 10% fetal bovine serum (FBS) and 100 U·ml^{-1} of penicillin. Our cell lines were bought from American Type Culture Collection (ATCC). The base medium for this cell line (ATCC, CRL-7637^{TM}) is ATCC-formulated DMEM (ATCC, 30–2002). To make the complete growth medium and culture cells properly, we added the following components to the base medium: FBS (the most widely used serum-supplement for the *in vitro* cell culture of eukaryotic cells) to a final concentration of 10% following the manufacturer's recommendation. The penicillin (Hyclone, USA) was used to prevent bacterial contamination of cell cultures due to their effective combined action against gram-positive and gram-negative bacteria. Cells were incubated at 37 °C with humidified air and 5% CO_2. For sample preparation, cells were trypsinized and transferred to cover glass-bottom (confocal dish) and 60-mm Petri dishes. The nitrite concentration was determined using the Griess reagent (Molecular Probes).[21] The plasma plume was in contact with liquid layers (2 mm) of serum-free Hanks' balanced salt buffer solution (HBSS). This buffer solution (Hyclone, USA) used to maintain the osmotic pressure and pH in cells. The resonance frequency and gas flow rate were 846 MHz and 0.5 L/min, respectively. To investigate the response under different discharge conditions, in every case, the fixed

distance between the open end of electrodes and surface of liquids was 1 mm. The dish including cells (10^3 cells) was irradiated with the plasma (1–3 min), and samples of the liquids from dish after plasma treatment were taken using a 96-well plate. The absorbance at 548 nm was measured using a Versamax Microplate Reader (Molecular Devices). In order to quantify the nitrite concentrations, a calibration curve was prepared using the standard sodium nitrite solutions (Molecular Probes). The intracellular generation of reactive oxygen species (ROS) after plasma treatment was detected by fluorescence microscopy using 2′,7′-dichloro fluorescein diacetate (DCF-DA) (Molecular Probes), which diffuses into cells and is deacetylated by cellular esterases to nonfluorescent 2′, 7′-dichlorodihydrofluorescein (DCFH).[22] In the presence of ROS, DCFH is rapidly oxidized to highly fluorescent DCF. Cells (10^5 cells) in dishes were pretreated with 10 μM DCF-DA for 3 min at 37 °C in the dark. Then, cells were exposed to the plasma (and/or gas flow only) for 10 s and 20 s and incubated for 3 min. Fluorescence-activated cells were detected and analyzed using a fluorescence microscope (Nikon TS100-F).

IV. CHARACTERIZATION AND APPLICATION

A. Plasma plume and gas temperature

Figure 6(a) represents the variation of plasma plume as a function of the input power at the gas flow rate of 8.0 L·min^{-1}. The resonant frequency of the device with the plasma load was 823 MHz, where the maximum power can be delivered from the power supply to the TPWR. An increase in the input power results in the enhancement of the electric field intensity at the open end of the TPWR, which in turn increases the power deposition to the plasma and consequently causes an increase in the plasma volume in the direction parallel to the electrode of the resonator. Figure 6(b) presents the variation of plasma plume as a function of the gas flow rate at an input power of 1.61 W. The plasma volume did not change much with the gas flow rate. However, as can be noted from the dotted lines in the figure, with a decrease in the gas flow rate, the position of the plasma was moved farther from the open end where the electric field is expected to be the highest. This could be attributed by a complex gas flow within the acrylic case in a lower gas flow regime. Figures 6(c) and 6(d) show the dependence of gas temperatures on the input power and gas flow rate, respectively. The gas temperature was measured 1 mm below the open end of TPWR. As can be seen in the figures, T_G was affected by P_{IN} and Ar gas flow rate F_{Ar}. As shown in Fig. 6(c), the increase in P_{IN} caused a continuous increase in T_G. At a gas flow rate of 2.0 L·min^{-1}, the gas temperature increases from 39.5 to 46 °C as the input power is increased from 1.6 W to 4.9 W. The measured T_G values are comparable to those of the CTLR microwave source.[7,12] An increase in P_{IN} led to an increase in gas heating, which is immediately followed by an increase in the plasma volume. In Fig. 6(d), the input power was kept constant at approximately 2.58 W for all gas flow rates. T_G was found to decrease as F_{Ar} was increased; this trend seems to be mainly attributed to an increase in the collision frequency of hot plasma species with the surrounding cold molecules.[23] These results indicate that the plume temperature can be adjusted effectively by controlling F_{Ar}. The plasma remained at room temperature at $F_{Ar} > 1.0$ L·min^{-1}, which is desirable for biomedical applications.

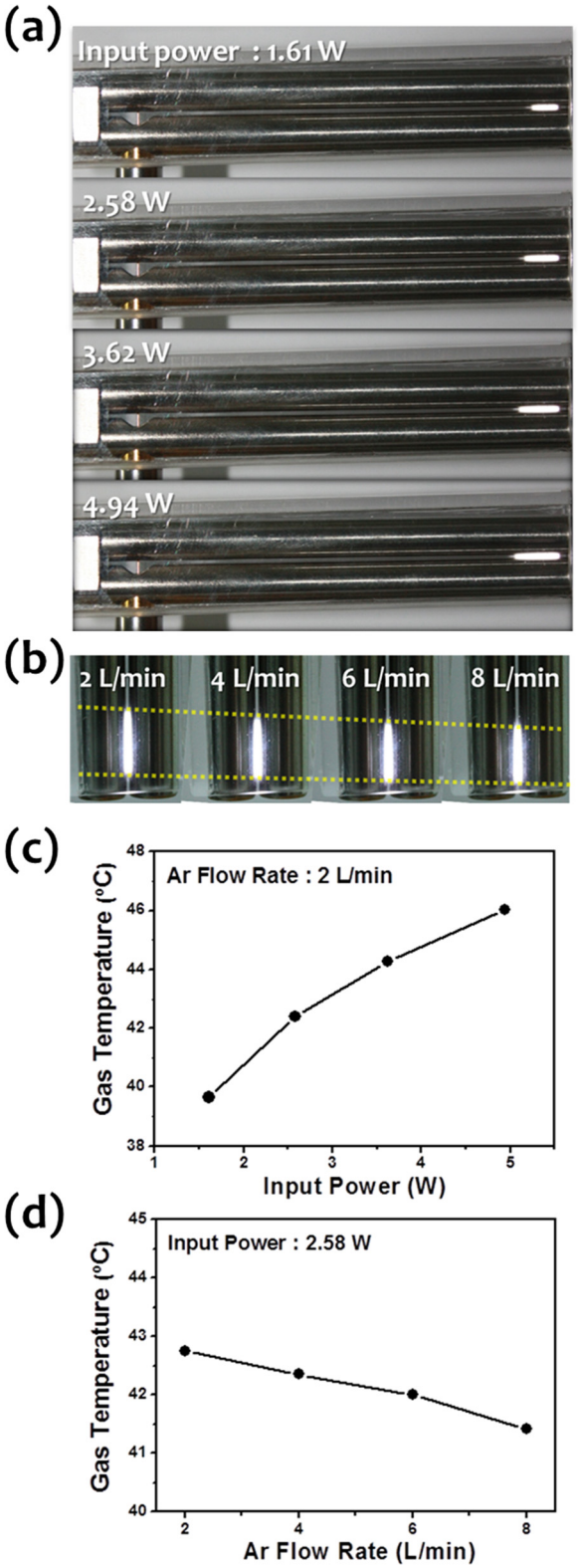

FIG. 6. (a) Variation of plasma plume as a function of the input power at a gas flow rate of 8.0 L·min^{-1} (b) Variation of plasma plume as a function of the gas flow rate at an input power 1.61 W. The dependence of gas temperatures on input power (c) and gas flow rate (d). The gas temperature was measured 1 mm below the open end of TPWR.

B. Electron excitation temperature and OH rotational temperature

To identify reactive species that are generated in the discharge and subsequently expelled with the gas flow, optical emission spectra were recorded in the wavelength range of $200\,\text{nm} \le \lambda \le 1000\,\text{nm}$ (Fig. 7). In this case, to identify the plasma species incident to the samples, the optical probe was placed at 15 mm below the open end along the wire axis. The strongest emission was the N_2^* band at 337.1 nm ($C^3\,\Pi_u \rightarrow B^3\,\Pi_g$), but many nitrogen lines, excited Ar atom lines ($2p-1s$), and excited oxygen lines were also observed. The N_2^+ band at 391 nm ($B^2\sum_u^+ \rightarrow X^2\sum_g^+$) was weak compared to that from helium jets. The emission spectrum clearly indicates a relatively strong emission from reactive species such as OH (309 nm) and NO (283 nm). The OH radicals are produced from water vapor in the Ar flow, which is humidified by water adsorbed on the inner surface of the argon line and the wire tube. The presence of the nitric oxide (NO) line at 283 nm is due to chemical conversion of N and O_2 (or N and O). These highly reactive species such as O, OH, and NO are considered to be the most effective agents in attacking cells or organic materials in general.

Especially (although not shown in figures), the intensity from the reactive species OH was nearly linearly related to the power dissipated in the discharge. A given emission intensity from a species can be regarded as a measure of the concentration of the species for a qualitative analysis. Therefore, operation at high P_{IN} may increase the richness of these reactive species.

T_G can also be inferred from the rotational temperature T_R of diatomic species, which is expected to be in equilibrium with T_G in atmospheric-pressure plasmas. Microwave-excited plasmas usually have a very large gradient of the gas temperature. In the core of the bulk plasma region, the gas temperature can be assumed to be comparable to the rotational temperature of OH or N_2^+ molecules. However, just at a few mm away from the plasma core, the gas temperature rapidly drops nearly to room temperature. To obtain the rotational temperature of OH, the simulated spectral profiles of OH, obtained from the simulation program (Rotem2 from Ref. 24), are compared with the measured ones, as shown in Fig. 8. To obtain the best fit between the experimental and the synthetic spectral bands, a least-square procedure was used. The fine structure of the rotational band of OH ($A\,^2\sum^+ \rightarrow X^2\Pi$ transition) from 306 nm and 310 nm was fitted to obtain T_G. The simulated spectrum at $720 \le T_R \le 750\,\text{K}$ gave the best fit to the experimental spectrum, whereas the apparent temperature of the plasma jet remained $\lesssim 325\,\text{K}$, which is compatible with biomedical applications.

Figure 9(a) presents the emission spectrum (obtained via a monochromator/PMT) from 390 nm to 900 nm observed in Ar ME-APPJ (5.4 W, 0.5 L·min^{-1}). In this case, to capture the plasma properties, the orientation of the optical probe was perpendicular to the wire axis. There exist many Ar $3p \rightarrow 1s$ peaks at 394.9 nm, 404.4 nm, 415.9 nm, 420.1 nm, 427.7 nm, and 434.5 nm and many $2p \rightarrow 1s$ peaks at 750.4 nm, 696.5 nm, 706.7 nm, 738.3 nm, 750.4 nm, 763.5 nm, 794.8 nm, 801.4 nm, 811.5 nm, 826.5 nm, and 842.5 nm. From the measurement of intensity and λ, the Boltzmann plot was obtained [Fig. 9(b)]. As can be seen in Fig. 9(b), the Ar population distribution over the energy levels is compatible with the Boltzmann distribution in our experimental conditions. Therefore, the Boltzmann-plot method can be used to calculate the electron excitation temperature T_{EXC} for the TPWR ME-APPJ. The T_{EXC} value was determined using from the selected Ar $2p-1s$ and $3p-1s$ transition lines. Because T_{EXC} may be used as a rough indication of the electron temperature,[25] these results suggest that the TPWR ME-APPJ can achieve higher mean electron energy than that in low-frequency APPJs. The calculated T_{EXC} was in the range of 0.5 ~1.2 eV. The change in P_{IN} did not affect T_{EXC} much [Fig. 9(c)], but a decrease in F_{Ar} caused a slight decrease in T_{EXC} [Fig. 9(d)], possibly due to an effective increase in the air mixing, which causes an increase in the frequency of electron-neutral collisions.

C. Electron density measurements by Stark broadening

Spontaneous emission lines emitted by the plasma are broadened by various mechanisms. For plasmas at atmospheric pressure with moderate electron density and temperature, the most important broadening mechanisms are the

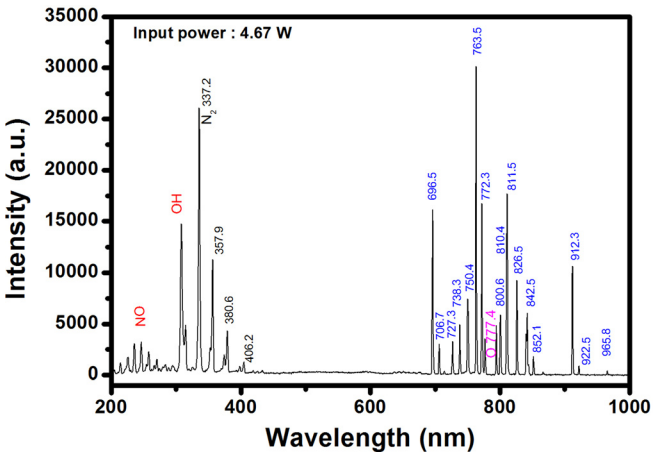

FIG. 7. Emission spectrum taken at 15 mm below the open end of Ar TPWR ME-APPJ (4.67 W and 0.5 L·min^{-1}).

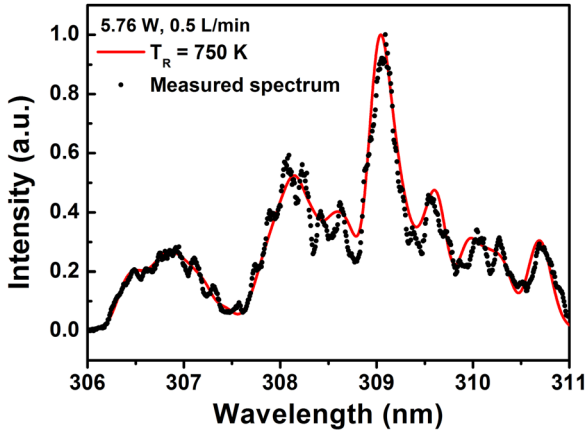

FIG. 8. Measured and simulated optical emission spectra around the OH line at 309.6 nm to determine the rotational temperature. For a simulated spectrum, the instrumental broadening of 0.2 nm is used.

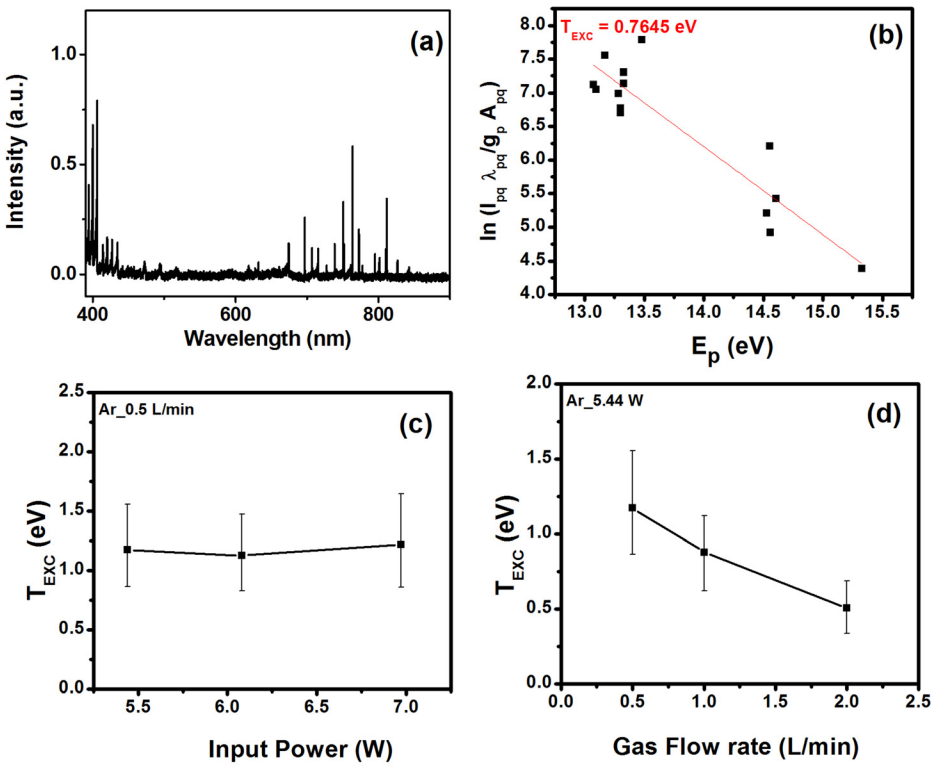

FIG. 9. (a) Emission spectra from 390 nm to 900 nm observed in Ar ME-APPJ (5.4 W, 0.5 L·min^{-1}). (b) Boltzmann plot method to estimate the excitation temperature. The electron excitation temperature as a function of (c) input power and (c) gas flow rate is also shown.

Stark broadening, Doppler broadening, and van der Waals broadening.[26] The characteristic instrumental function of the optical system causes line broadening called instrumental broadening. The total broadening of the line profile is due to the combined contribution of all causes. Stark and van der Waals mechanisms have a Lorentzian profile. The Doppler broadening and the instrumental broadening have a Gaussian profile. The convolution of the Gaussian and Lorentzian components results in a Voigt profile.

The electron density can be determined using the optical emission spectroscopy (OES) of the line shape of the Balmer transition (4–2) of atomic hydrogen at 486.13 nm (H_β line).[27]

For a given T_G and gas density, the full-width at half-maximum (FWHM) of van der Waals broadening ($\Delta\lambda_{vdw}$) and Doppler broadening ($\Delta\lambda_D$) can be calculated.[27–29] The effect of Doppler broadening has been determined using the following expression: $\Delta\lambda_D = 7.16 \times 10^{-7}\ \lambda\ (T_G/M)^{1/2}$ (λ is the wavelength in Å, T_G is the gas temperature in K, and M is the atomic weight in g mol^{-1}), and van der Waals broadening profiles are related to the gas pressure p and temperature T_G.[27]

The H_β spectral line profile [Fig. 10(a)] was measured in Ar TPWR ME-APPJ, and the Voigt profile was fitted to the experimental points [Fig. 10(b)]. The fitting was made using the Voigt function with a Gaussian line width of 0.23 nm [in

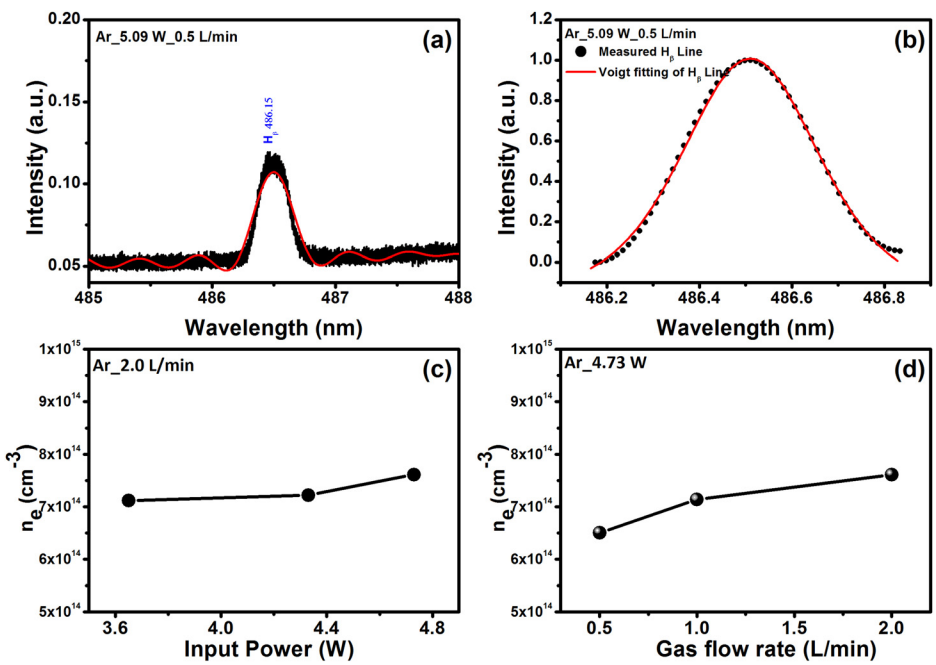

FIG. 10. (a) Measured H_β line profile (the red curve represents the low-pass noise filtered signal) and (b) the Voigt function add to the normalized line profile points for Ar ME-APPJ with an input power of 5 W and a gas flow rate of 2 L·min^{-1}. The electron density obtained from Stark broadening as a function of (c) input power and (d) gas flow rate is also shown.

our typical case, $\Delta\lambda_I = 0.22$ nm, $\Delta\lambda_D = 0.01$ nm ($T_G = 750$ K), $\Delta\lambda_V$ (FWHM of the Voigt profile) = 0.36 nm]. The shape and the FWHM of the instrumental broadening $\Delta\lambda_I$ were deduced by recording the Ne line (633 nm) emitted by a He–Ne laser. The resulting value of the FWHM of the Lorentzian profile $\Delta\lambda_L$ ($= \Delta\lambda_{vdw} + \Delta\lambda_S$) enabled us to calculate the electron number density n_e in the Ar plasma by the formula of the GKS theory or of the Gig-Card theory.[29] We can simply use the $\Delta\lambda_S$ (nm) of Stark broadening which is related to n_e (cm^{-3}) by[28]

$$\Delta\lambda_S = 2.0 \times 10^{-11} n_e^{2/3}.$$

In our typical case, we have $\Delta\lambda_L = 0.21$ nm and $\Delta\lambda_{vdw} = 0.057$ nm, and then, we obtain $\Delta\lambda_s = 0.151$ nm. Calculated n_e using the data from Ref. 28 has a value of 6.6×10^{14} cm^{-3}, and it is observed to increase slowly as P_{IN} increased [Fig. 10(c)]; this trend is correlated with the increase in the plasma column length (Fig. 5). Calculated n_e increased from 6.5×10^{14} to 7.6×10^{14} cm^{-3} as F_{Ar} increased from 0.5 to 2.0 L·min^{-1} [Fig. 10(d)]. The calculated values of n_e are comparable to those of similar types of microwave sources.[27,29]

D. OH concentrations by the TA method

The plasma was ignited, and the TA solution was exposed to the effluent. The resonance frequency and gas flow rate were 846 MHz and 0.5 L/min, respectively. To investigate the response under different discharge conditions, in every case, the fixed distance between the open end of electrodes and surface of liquids was 1 mm. The fluorescence intensity increased after reaction with the plasma; the change was used to estimate the quantity of OH radicals trapped by TA. The fluorescence intensity corresponds to a time-integrated OH radical concentration in the liquid. Figure 11 shows the fluorescence spectra of HTA as functions of treatment times (0, 1, 3, 5, 7, and 10 min) and input powers (4.11 and 4.66 W). As treatment time elapsed, the fluorescence intensity increased [Fig. 11(a)]; this change indicates an increase in the total amount of OH radicals trapped by TA.[30] The 2HTA concentration increased nearly linearly with treatment time [Fig. 11(b)]. The calculated OH radical density in the solution was comparable to that obtained by high-voltage (up to 20 kV) pulsed discharge.[30] The fluorescence spectra of HTA as functions of P_{IN} [Fig. 11(c)] indicate that the OH concentration increased with P_{IN}, in agreement with the previous measurement of the OH density.[20]

E. Plasma-cell interactions

Reactive nitrogen species are also formed in the liquid phase. Figure 12 shows the results of the nitric oxide (NO) quantitation assay performed on HBSS buffer solution after plasma treatment. No significant difference is observed in gas-treated control liquids. On the other hand, the nitrite concentration increased after plasma exposure with increasing treatment times (1–3 min) and input powers (2.7, 3.7, and 5.7 W) [Fig. 12(a)]. It is observed that the concentration in the presence of melanoma cells is higher than that in the absence of cells [Fig. 12(b)]. This suggests that the plasma can influence NO production not only in the liquids but also in the cells, indicating that the plasma-activated buffer solution affects cell response. The plasma-induced radicals in the gas phase may be transported into and react with the buffer solution and, finally, interact with the biological systems of the cells.[31]

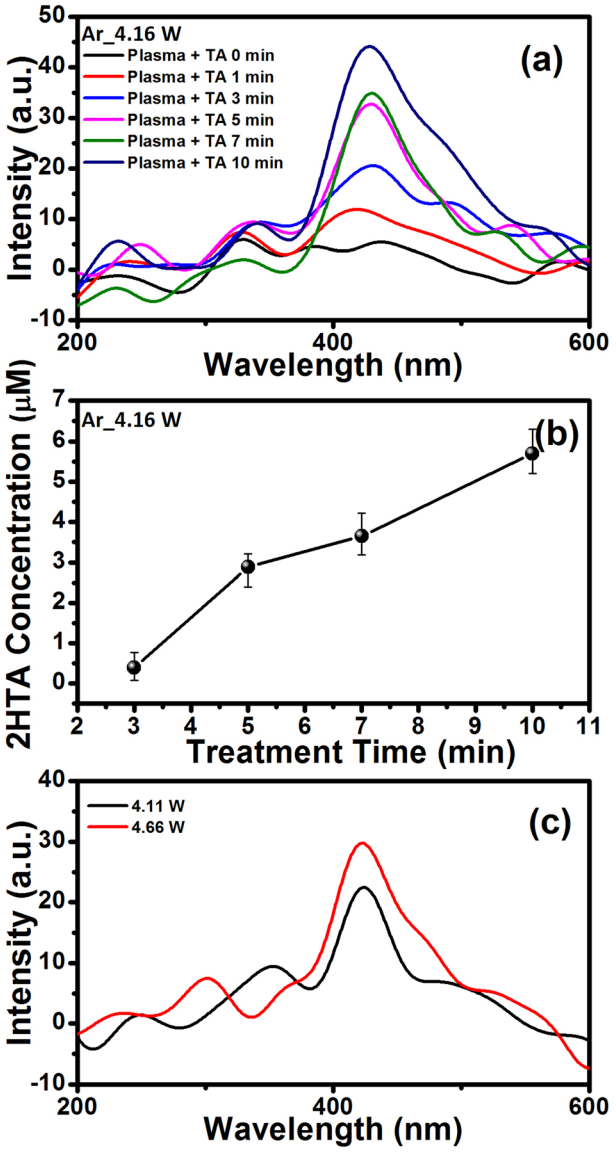

FIG. 11. (a) Fluorescence spectra of aqueous TA solutions exposed to the ME-APPJ for different treatment times (0, 1, 3, 5, 7, and 10 min) (open end-to-liquid surface distance, 1 mm; the input power, 4.16 W). (b) 2HTA concentration obtained by plasma treatment to a TA solution as a function of treatment time (input power, 4.16 W). (c) The dependence of fluorescence spectra on input power (4.11 and 4.66 W) (treatment time; 5 min).

In order to examine the plasma-induced intracellular response, we used a permeable fluorescence probe (DCF-DA). In ROS observation, we marked points on a dish and treated those points for 10 s and 20 s with the plasma. The production of ROS was observed in those marked points. Figure 13 shows the photograph of the plasma plume [Fig. 13(a), input power: 5.7 W] with dish containing cells (HBSS, layer 2 mm) during treatment and the fluorescence images of intracellular ROS generation induced by plasma exposure

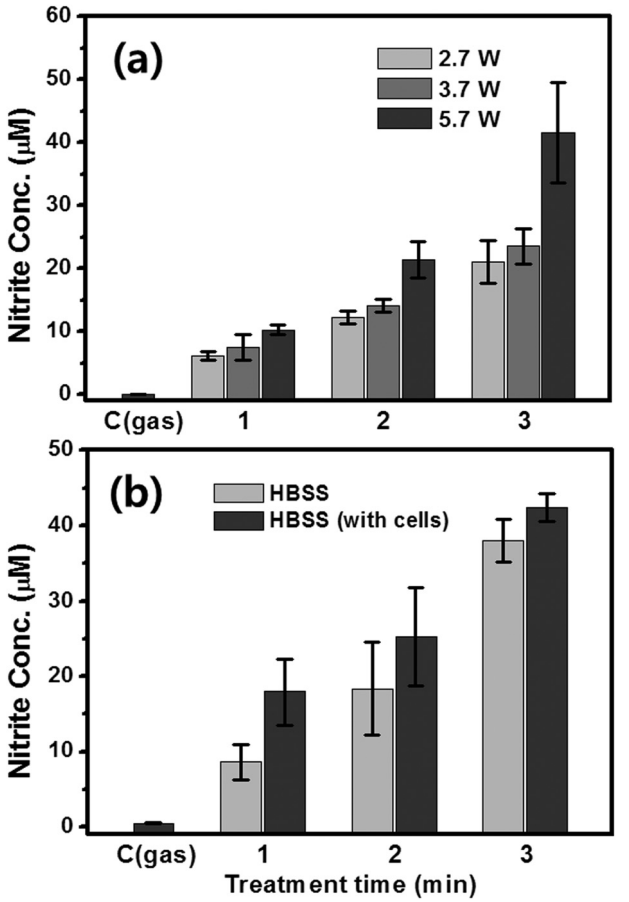

FIG. 12. Nitrite concentration as a function of treatment times (1–3 min) and (a) input powers (2.7, 3.7, and 5.7 W) and (b) in the presence and absence of cells (5.7 W) (each point represents the mean ± SD of three replicates). The treatment time for the gas-treated control was 3 min.

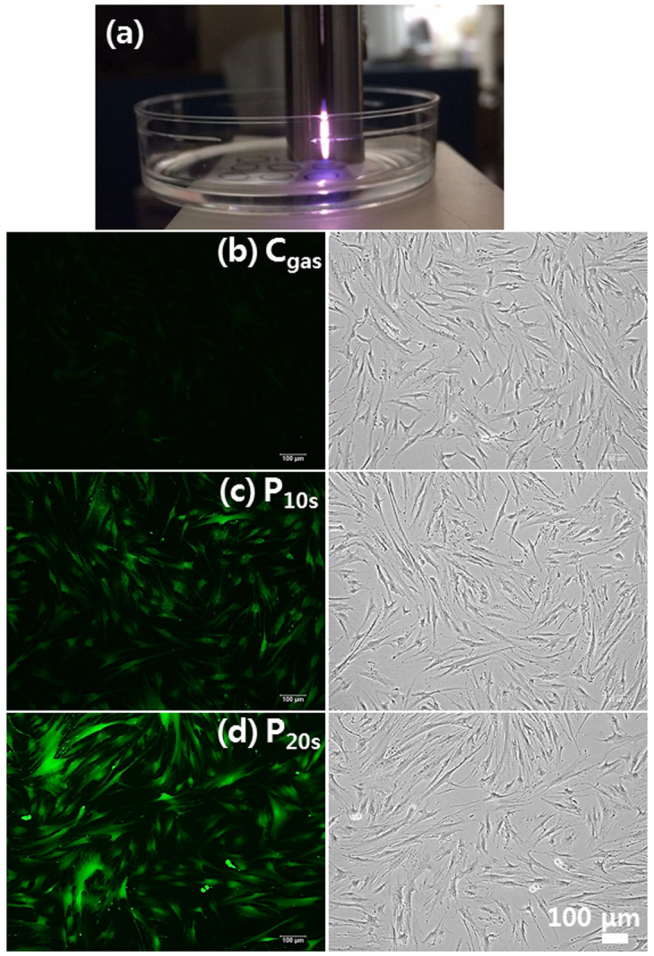

FIG. 13. (a) Photograph of the plasma plume during treatment and fluorescence images of intracellular ROS production and bright field images: (b) gas-treated control cells (for 20 s), (c) plasma-treated cells (for 10 s), and (d) plasma-treated cells (for 20 s). The input power is 5.7 W. The scale bar is 100 μm.

with bright field images in melanoma cells. The intensity level of the fluorescence was higher than that of gas-treated cells [Figs. 13(b) and 13(c)]. The plasma-treated cell populations containing high levels of DCF fluorescence were dramatically increased with increasing exposure time [Fig. 13(d)]. In comparison to the intracellular ROS production in the cells treated by low-frequency APPJs,[32,33] Ar TPWR ME-APPJ appears to cause a larger intracellular ROS production. This might be attributed to the increased electron density in the generated microwave plasma. Reactive oxygen species such as hydroxyl radicals (·OH) detected in liquids by the TA method (Fig. 11), and nitric oxide (Fig. 12) could cause this cellular response. Plasma-activated liquids have been shown to be effective in clinical therapy.[34] Our newly developed ME-APPJ may be a useful tool with high electron density to activate liquids for clinical applications such as targeting objects inside the body.

V. CONCLUSION

A microwave-excited atmospheric pressure plasma jet (ME-APPJ) was generated by using a quarter-wavelength two-parallel-wire transmission line resonator (TPWR). The device has a simple structure and sustains stable ME-APPJ due to the narrow gap of electrodes with $Z_0 = 50\,\Omega$. The experiments were performed with $1 \le P_{IN} \le 6$ W and $0.5 \le F_{Ar} \le 8.0\,\text{L·min}^{-1}$. T_G increased with an increase in P_{IN} and decreased with an increase in F_{Ar} and in distance from the open end of TPWR. T_{EXC} was 0.5 ~1.2 eV, and T_R of the OH band (306–311 nm) was 720 ~750 K, and these were nearly independent of P_{IN}. n_e was 6.5×10^{14}–$7.6 \times 10^{14}\,\text{cm}^{-3}$, depending on P_{IN} and F_{Ar}. The jet has characteristics of low-temperature jets; the trait is important for the treatment of surfaces that are sensitive to elevated temperatures while producing abundant reactive species. This device can also be operated at low flows of the working gas and at low power, which are well-suited for biomedical applications. The plasma from ME-APPJ using TPWR was used to treat cancer cells; the results proved that ME-APPJ is effective and convenient for cell treatment.

ACKNOWLEDGMENTS

The authors thank Jeong Yeon Lee and Chan Hoon Ahn for their assistance. The authors are grateful to Professor Dae-Seong Kang of Dong-A University for his help. This work was supported by the National Research Foundation of Korea (NRF) under Grant Nos. 2016R1C1B1014508, 2015R1D1A1A09056870, and 2015R1C1A1A02036615, funded by the Korean government (MSIP).

[1]J. Winter, R. Brandenburg, and K.-D. Weltmann, "Atmospheric pressure plasma jets: An overview of devices and new directions," Plasma Sources Sci. Technol. **24**, 064001 (2015).
[2]S. J. Park, J. Choi, G. Y. Park, S. K. Lee, Y. Cho, J. I. Yun, S. Jeon, K. T. Kim, J. K. Lee, and J. Y. Sim, "Inactivation of S. mutans using an atmospheric plasma driven by a palm-size-integrated microwave power module," IEEE Trans. Plasma Sci. **38**, 1956 (2010).
[3]S. Schneider, F. Jarzina, J.-W. Lackmann, J. Golda, V. Layes, V. S. Gathen, J. E. Bandow, and J. Benedikt, "Summarizing results on the performance of a selective set of atmospheric plasma jets for separation of photons and reactive particles," J. Phys. D: Appl. Phys. **48**, 444001 (2015).
[4]M. Keidar, "Plasma cancer treatment," Plasma Sources Sci. Technol. **24**, 033001 (2015).
[5]R. Miotk, B. Hrycak, D. Czylkowski, M. Dors, M. Jasinski, and J. Mizeraczyk, "Liquid fuel reforming using microwave plasma at atmospheric pressure," Plasma Sources Sci. Technol. **25**, 035022 (2016).
[6]A. R. Hoskinson, A. Yared, and J. Hopwood, "Gas heating and plasma expansion in pulsed microwave-excited microplasmas," Plasma Sources Sci. Technol. **24**, 055002 (2015).
[7]H. W. Lee, S. K. Kang, I. H. Won, H. Y. Kim, H. C. Kwon, J. Y. Sim, and J. K. Lee, "Distinctive plume formation in atmospheric Ar and He plasmas in microwave frequency band and suitability for biomedical applications," Phys. Plasmas **20**, 123506 (2013).
[8]K. McKay, F. Iza, and M. G. Kong, "Excitation frequency effects on atmospheric-pressure helium RF microplasmas: Plasma density, electron energy and plasma impedance," Eur. Phys. J. D **60**, 497 (2010).
[9]J. Gregório, A. R. Hoskinson, and J. Hopwood, "Modeling of microplasmas from GHz to THz," J. Appl. Phys. **118**, 083305 (2015).
[10]H. W. Lee, G. Y. Park, Y. S. Seo, Y. H. Im, S. B. Shim, and H. J. Lee, "Modelling of atmospheric pressure plasmas for biomedical applications," J. Phys. D: Appl. Phys. **44**, 053001 (2011).
[11]F. Iza and J. Hopwood, "Split-ring resonator microplasma: Microwave model, plasma impedance and power efficiency," Plasma Sources Sci. Technol. **14**, 397 (2005).
[12]J. Choi, F. Iza, H. J. Do, J. K. Lee, and M. H. Cho, "Microwave-excited atmospheric-pressure microplasma based on a coaxial transmission line resonator," Plasma Sources Sci. Technol. **18**, 025029 (2009).
[13]Z. B. Zhang and J. Hopwood, "Linear arrays of stable atmospheric pressure microplasmas," Appl. Phys. Lett. **95**, 161502 (2009).
[14]S. K. Kang, Y. S. Seo, H. Wk, Lee, Aman-ur-Rehman, G. C. Kim, and J. K. Lee, "Slit shaped microwave induced atmospheric pressure plasma based on a parallel plate transmission line resonator," J. Phys. D: Appl. Phys. **44**, 435201 (2011).
[15]B. C. Wadell, *Transmission Line Design Handbook* (Artech House, 1991), p. 66.
[16]J. Choi, A.-A. H. Mohamed, S. K. Kang, K. C. Woo, J. T. Kim, and J. K. Lee, "900-MHz nonthermal atmospheric pressure plasma jet for biomedical applications," Plasma Processes Polym. **7**, 258 (2010).
[17]See http://www.comsol.com for Comsol Multiphysics.
[18]X. Y. Liu, X. K. Pei, K. Ostrikov, X. P. Lu, and D. W. Liu, "The production mechanisms of OH radicals in a pulsed direct current plasma jet," Phys. Plasmas **21**, 093513 (2014).
[19]P. Lukes, E. Dolezalova, I. Sisrova, and M. Clupek, "Aqueous-phase chemistry and bactericidal effects from an air discharge plasma in contact with water: Evidence for the formation of peroxynitrite through a pseudo-second-order post-discharge reaction of H_2O_2 and HNO_2," Plasma Sources Sci. Technol. **23**, 015019 (2014).
[20]K. Ninomiya, T. Ishijima, M. Imamura, T. Yamahara, H. Enomoto, K. Takahashi, Y. Tanaka, Y. Uesugi, and N. Shimizu, "Evaluation of extra- and intracellular OH radical generation, cancer cell injury, and apoptosis induced by a non-thermal atmospheric-pressure plasma jet," J. Phys. D: Appl. Phys. **46**, 425401 (2013).
[21]A. R. Gibson, H. O. McCarthy, A. A. Ali, D. O'Connell, and W. G. Graham, "Interactions of a non-thermal atmospheric pressure plasma effluent with PC-3 prostate cancer cells," Plasma Processes Polym. **11**, 1142 (2014).
[22]T. M. Johnson, Z. X. Yu, V. J. Ferrans, R. A. Lowenstein, and T. Rinkel, "Reactive oxygen species are downstream mediators of p53-dependent apoptosis," Proc. Natl. Acad. Sci. U.S.A. **93**, 11848 (1996).
[23]M. Klas and S. Ptasinska, "Characteristics of N_2 and N_2/O_2 atmospheric pressure glow discharges," Plasma Sources Sci. Technol. **22**, 025013 (2013).
[24]S. Y. Moon and W. Choe, "A comparative study of rotational temperatures using diatomic OH, O_2 and N_2^+ molecular spectra emitted from atmospheric plasmas," Spectrochim. Acta, Part B **58**, 249 (2003).
[25]J. L. Walsh and M. G. Kong, "Contrasting characteristics of linear-field and cross-field atmospheric plasma jets," Appl. Phys. Lett. **93**, 111501 (2008).
[26]J. Torres, J. M. Palomares, A. Sola, J. J. A. M. van derMullen, and A. Gamero, "A Stark broadening method to determine simultaneously the electron temperature and density in high-pressure microwave plasmas," J. Phys. D: Appl. Phys. **40**, 5929 (2007).
[27]G. Wattieaux, M. Yousfi, and N. Merbahi, "Optical emission spectroscopy for quantification of ultraviolet radiations and biocide active species in microwave argon plasma jet at atmospheric pressure," Spectrochim. Acta Part B **89**, 66 (2013).
[28]X.-M. Zhu, W.-C. Chen, and Y.-K. Pu, "Gas temperature, electron density and electron temperature measurement in a microwave excited microplasma," J. Phys. D: Appl. Phys. **41**, 105212 (2008).
[29]B. Hrycak, M. Jasiński, and J. Mizeraczy, "Spectroscopic investigations of microwave microplasmas in various gases at atmospheric pressure," Eur. Phys. J. D **60**, 609 (2010).
[30]S. Kanazawa, H. Kawano, S. Watanabe, T. Furuki, S. Akamine, R. Ichiki, T. Ohkubo, M. Kocik, and J. Mizeraczyk, "Observation of OH radicals produced by pulsed discharges on the surface of a liquid," Plasma Sources Sci. Technol. **20**, 034010 (2011).
[31]S. Iseki, K. Nakamura, M. Hayashi, H. Tanaka, H. Kondo, H. Kajiyama, H. Kano, F. Kikkawa, and M. Hori, "Selective killing of ovarian cancer cells through induction of apoptosis by nonequilibrium atmospheric pressure plasma," Appl. Phys. Lett. **100**, 113702 (2012).
[32]H. M. Joh, S. J. Kim, T. H. Chung, and S. H. Leem, "Reactive oxygen species-related plasma effects on the apoptosis of human bladder cancer cells in atmospheric pressure pulsed plasma jets," Appl. Phys. Lett. **101**, 053703 (2012).
[33]S. J. Kim and T. H. Chung, "Plasma effects on the generation of reactive oxygen and nitrogen species in cancer cells in-vitro exposed by atmospheric pressure pulsed plasma jets," Appl. Phys. Lett. **107**, 063702 (2015).
[34]F. Utsumi, H. Kajiyama, K. Nakamura, H. Tanaka, M. Mizuno, K. Ishikawa, H. Kondo, H. Kano, M. Hori, and F. Kikkawa, "Effect of indirect nonequilibrium atmospheric pressure plasma on anti-proliferative activity against chronic chemo-resistant ovarian cancer cells in vitro and in vivo," PLoS ONE **8**, e81576 (2013).